



HAL
open science

Engraving Depth-Controlled Nanohole Arrays on Fused Silica by Direct Short-Pulse Laser Ablation

Xin Liu, Raphaël Clady, David Grojo, Olivier Utéza, Nicolas Sanner

► **To cite this version:**

Xin Liu, Raphaël Clady, David Grojo, Olivier Utéza, Nicolas Sanner. Engraving Depth-Controlled Nanohole Arrays on Fused Silica by Direct Short-Pulse Laser Ablation. *Advanced Materials Interfaces*, 2023, 10 (7), pp.2202189. 10.1002/admi.202202189 . hal-04241493

HAL Id: hal-04241493

<https://hal.science/hal-04241493>

Submitted on 13 Oct 2023

HAL is a multi-disciplinary open access archive for the deposit and dissemination of scientific research documents, whether they are published or not. The documents may come from teaching and research institutions in France or abroad, or from public or private research centers.

L'archive ouverte pluridisciplinaire **HAL**, est destinée au dépôt et à la diffusion de documents scientifiques de niveau recherche, publiés ou non, émanant des établissements d'enseignement et de recherche français ou étrangers, des laboratoires publics ou privés.

Engraving Depth-Controlled Nanohole Arrays on Fused Silica by Direct Short-Pulse Laser Ablation

Xin Liu, Raphaël Clady, David Grojo, Olivier Utéza, and Nicolas Sanner*

Periodic nanohole arrangements constitute an important building block of advanced photonic devices. Aside from standard nanofabrication tools, a direct laser-based approach is introduced here, that enables single-step and point-by-point machining of arrays of holes with subwavelength diameters and depths reaching several micrometers at the surface of fused silica. The method relies on a simple optical arrangement including an axicon combined with an amplitude mask to shape the laser intensity in appropriately truncated micro-Bessel beams of adjustable length. The suitability and limitations of the technique are investigated to fabricate arrays of cylindrical nanoholes with tunable depths. In particular, the challenge of avoiding crosstalk effects during the laser-writing process of high-density arrays is explored. The achievability of square arrays of nanoholes at the surface of fused silica, with diameters down to 200 nm and variable depths from 3 to 20 μm at a spatial density defined by a pitch of 1.5 μm is demonstrated. The performance level shows the potential of the direct-laser-processing method towards the realization of integrated devices, offering a highly flexible and cost-effective alternative technique to current nanofabrication methods.

1. Introduction

Arrays of nanoholes with a controllable period, diameter, and depth at the surface of materials are of high interest for a large range of applications in physics, chemistry, and material science. Implemented on thin metallic films, they lead to a wide variety of unexpected optical properties^[1] resulting from sur-

face plasmon resonances, and fostered the development of advanced sensors.^[2,3] Fabricated on dielectric materials, arrays of nano-holes – and more generally regularly-ordered structures composed of subwavelength-diameter holes – form the basis of the architecture of integrated two-dimensional photonic crystals and all-dielectric metasurfaces, able to confine and manipulate light at unprecedented levels (including amplitude, spectral and spatial management).^[4] The usual technological approaches for such nanofabrication of both plasmonic and all-dielectric nanostructures rely on various tools and approaches, amongst which focused ion beam, electron beam, photolithography, reactive ion etching, etc.^[5,6] These fabrication methods are mature and highly performant, however, they are slow and they require several steps and techniques that need to be optimized for each material used, thereby inevitably increasing the

overall costs and complexity of the whole process.

Future advanced devices are now calling for making use of the third dimension (Z) in addition to perfectly well controlled planar nanopatterns (in X and Y dimensions).^[7] In particular, arrangements made of arrays of nanoholes with depths reaching at least several micrometers may greatly broaden the range of possible designs and functionalities of nanophotonic structures.^[7,8] However, the technological fabrication of such deep holes with a cylindrical profile at the surface of materials is challenging.^[9–12] Thus, introducing a versatile fabrication technique that adds the hole depth as a straightforward and independent degree of freedom holds promises to form advanced architectures. In this context, we explore ultrafast laser processing as a direct way to create deep air holes at the surface of a reference dielectric material, fused silica. By “direct” we mean that one hole is fabricated by a single-step process, consisting in only one laser shot to ablate matter, without any extra treatment (like chemical etching for example^[13]) nor translation of the target material.^[14] Although the ultimate spatial resolution of direct laser ablation with ultrashort pulses has not reached yet sufficient performance standards to compete with traditional nanofabrication processes to fabricate functional nanophotonic components, our aim is to show it represents a route for an alternative and complementary solution with attractive advantages in terms of speed, maskless and single-step process, absence of need of vacuum environment or chemicals. Additionally, the nanostructures can be fabricated on a single

X. Liu, R. Clady, D. Grojo, O. Utéza, N. Sanner
Aix Marseille Univ., CNRS, LP3, UMR7341
Marseille 13288, France
E-mail: nicolas.sanner@univ-amu.fr

X. Liu
State Key Laboratory of Transient Optics and Photonics
Xi'an Institute of Optics and Precision Mechanics of CAS
Xi'an 710119, P. R. China

 The ORCID identification number(s) for the author(s) of this article can be found under <https://doi.org/10.1002/admi.202202189>.

© 2023 The Authors. Advanced Materials Interfaces published by Wiley-VCH GmbH. This is an open access article under the terms of the Creative Commons Attribution License, which permits use, distribution and reproduction in any medium, provided the original work is properly cited.

DOI: 10.1002/admi.202202189

material (fused silica here, used as a model glass substrate), thus playing both roles of substrate and constituent material, without requiring separate deposition and etching sequences of different dielectric/semiconductor materials.^[15] For photonic applications, the low refractive index of fused silica just needs to be compensated by increasing the structure lengths, that is readily provided by directly fabricating several-micrometers-deep holes, without requiring tedious multistep cycles for 3D processing.

Laser processing approaches for the fabrication of regular patterns composed of subwavelength features have already been explored, but mainly non-direct ones. They are based either on i) matter self-organization upon controlled accumulation of thousands of femtosecond laser shots,^[16–18] or ii) optical near-field super-resolution techniques that take advantage of the local enhancement of the laser electric field provided by, e.g., predeposition of microspheres^[19–20] or pre-processing of nanoholes^[21] on the sample surface. The feature size can reach the sub-100 nm scale and on relatively large areas, but these techniques give access only to shallow depths (<100 nm) and they are intrinsically nondigital. To give access to individual control of each elementary feature and provide the highest degree of agility, point-by-point direct writing is needed.

Direct ultrashort-pulse laser ablation of the materials surface has come to a level of maturity relevant to imprint individual features much smaller than the laser wavelength, reached mainly by careful adjustment of the laser pulse energy with respect to the ablation threshold.^[22–24] Writing an array of nanoholes one by one therefore offers an infinite freedom for designing any higher-complexity structures and architectures. However, accessing hole depths larger than few hundreds of nanometers is not straightforward for a Gaussian beam tightly focused on the material surface, due to the physics of the interaction between an ultrashort pulse and a transparent wide-bandgap dielectric material. Indeed, nonlinear absorption of laser photons followed by inverse Bremsstrahlung and subsequent collisional excitation create a fast buildup of a dense free-electron plasma during the laser pulse itself,^[25] that significantly alters the beam propagation (screening/reflection) below the surface.^[26,27] This yields to transient skin depths typically in the 100 nm range, and then ablation depths much shorter than the Rayleigh distance of the focused beam. As a result, small-aspect-ratio holes (depth/diameter < 1) or distorted hole shapes^[28] are obtained, that cannot be avoided unless complex temporal shaping^[29] or specific microfilamentation regimes^[30] are used. On the other hand, the processing of extremely long individual nanochannels with aspect ratios higher than 100:1 have been demonstrated using Bessel beams,^[31,32] that provide an interesting solution to obtain small-size core diameters on long distances. However, a gap exists between these two regimes. Fabricating nanoholes with an aspect ratio equal to few units (typically between 1 and 30) and well-controlled dimensions with on-demand tunability, that match the requirements for fabricating nanophotonic structures, has been poorly investigated so far. Thus, the laser-fabrication of dense arrays of such nanoholes at the surface of dielectric materials has not been demonstrated yet.

Here, we investigate experimentally this solution based on ultrafast laser ablation. We first present how we generate

a micro-Bessel beam with a truncation giving control on its length, irrespective of the core diameter. Then we irradiate fused silica surface to fabricate square arrays of nanoholes, with laser pulse energy and spatial periodicity as key varying parameters. A threshold-based analysis is presented, and a relevant processing range is identified. We also demonstrate that building arrays of nanoholes by juxtaposing individual ones is not straightforward, and we explore how the presence of the previously-engraved neighbor hole may perturb the processing of the next one. This defines limits observed experimentally and supported by numerical simulations. The assessment of these aspects is of major importance to propose perspective solutions towards further downscaling and denser packing and then develop efficient and suitable nanofabrication technologies based on this laser-processing method.

2. Experimental Section

2.1. Beam shaping

The experimental setup is depicted in **Figure 1a**. It is based on a Ti:Sa laser source, delivering 25 fs pulses at the central wavelength of 800 nm and with a linear polarization. The pulse duration is negatively chirped to 1 ps by adjusting the compressor of the laser chain, previously identified as the optimal conditions for processing high-quality craters.^[33] For generating a Bessel beam, the incident Gaussian beam of radius $W = 2.5$ mm at $1/e^2$ intensity propagates through an axicon,^[34,35] of base angle $\alpha = 1^\circ$, yielding a half-conical angle $\theta = \text{asin}(n \sin \alpha) - \alpha = 0.45^\circ$, with $n = 1.45$ the refractive index of the fused silica at the working wavelength. An annular aperture, placed just after the axicon, acts as an amplitude mask that limits the transverse width of the set of conical plane waves that interfere to form the Bessel beam, therefore enabling to tailor its length on demand. Then, a 4-f telescopic demagnifying system composed of a lens ($f_1 = 500$ mm) and a long-working-distance microscope objective (Mitutoyo Plan APO NIR 20x, NA = 0.4, $f_2 = 10$ mm) reduces the beam dimensions by a factor $\gamma = f_2/f_1 = 50$. The half-conical angle of the beam (in air) incident onto the sample is therefore $\theta' = \gamma\theta = 22.5^\circ$, corresponding to the one that would be obtained by an axicon of base angle $\alpha' = 36.1^\circ$. Before placing the workpiece in the beam path, the obtained micro-Bessel beam is imaged longitudinally plane by plane and reconstructed by stacking 2D images together, as shown in **Figure 1b**. Without the annular aperture, the beam intensity distribution shows a long central intense core surrounded by concentric lobes, as expected for a typical Bessel beam generated by such a technique (**Figure 1b**, 1st row). Now, introducing the annular aperture truncates the length of the Bessel beam^[36] (**Figure 1b**, 2nd row). In addition, by masking the tip of the axicon, this technologically-simple technique also offers the advantage of filtering out its fabrication imperfections, responsible of nonideal tapered shape of the obtained non-truncated Bessel beams,^[37] as observed experimentally (**Figure 1b**, 1st row). The diameter of the core of the truncated Bessel beam is unchanged, because the half-conical angle θ is the same as the non-truncated beam. Then, the relevant parameter to engineer the length z_B of the Bessel beam (irrespective of its diameter) is the width e of the

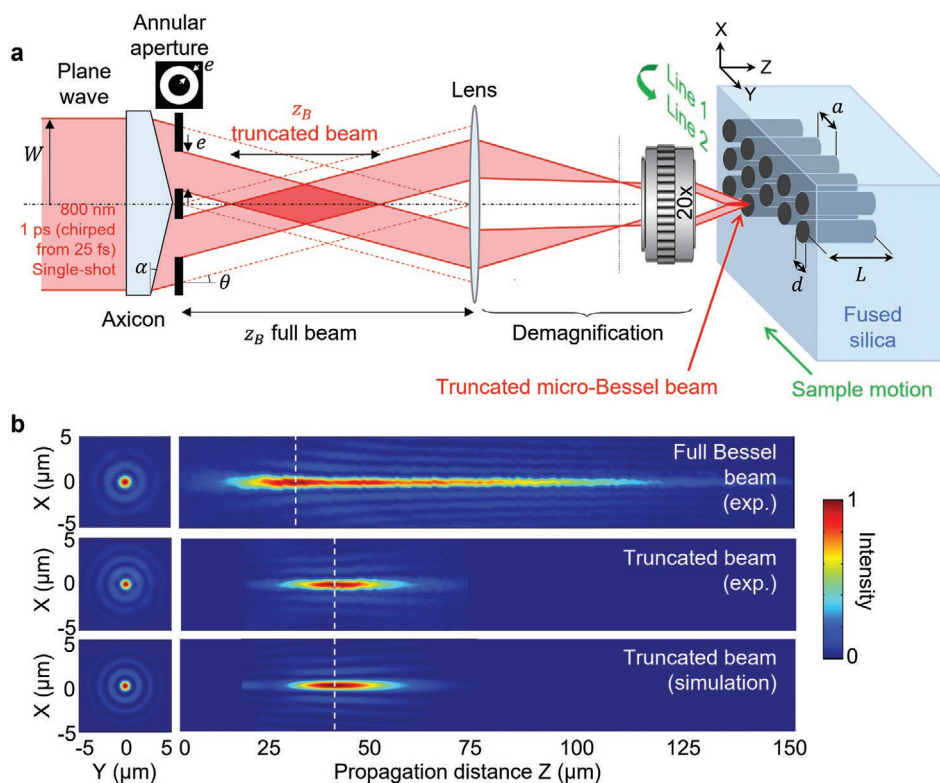


Figure 1. a) Schematics of the experiment. The laser beam is shaped by a combination of an axicon followed by an annular aperture, enabling to shorten the length of the obtained Bessel beam ($=$ length of the diamond-shaped red zone) while its core diameter is unchanged. After demagnification by a telescopic system composed of a lens and a microscope objective, the array of nanoholes is fabricated by processing holes one by one at the surface of the fused silica sample. b) Beam intensity distributions at the surface of the fused silica sample: the full Bessel beam without truncation (experimental – 1st row) and the truncated beam (experimental – 2nd row, and simulation – 3rd row) used for processing of the nanoholes. The transverse XY intensity maps represented on the left are taken at the coordinate Z of maximum beam intensity, represented by white dashed lines on the XZ intensity maps.

annular slit. Even if straightforward application of geometrical optics ($z_B = e/\tan \theta$) can help for dimensioning purposes, accurate analytical estimations^[36] or numerical calculations^[38] are required to set the optimal value of e , since strong modulations of intensity along Z may occur due to diffraction effects caused by such beam truncation. In our conditions, the optimal aperture of the annular slit is $e = 420 \mu\text{m}$, enabling to obtain a “focal line” of length $z_B = 21 \mu\text{m}$ with a smooth intensity profile along Z and a core diameter ($=$ first zero of intensity of the Bessel function) of $0.90 \mu\text{m}$ FWHM. This is perfectly reproduced by numerical simulations (Figure 1b, 3rd row). Note that technical details about the simulations are reported in Section 3.4, whereas Supporting Information Note 1 provides more details about beam truncation and optimization of the width of the annular aperture used.

2.2. Laser Processing

The experiments are carried out in ambient air. The fused silica sample is placed on a 3-axis motorized translation stage and its front surface is precisely positioned at the coordinate Z corresponding to the location of the peak intensity of the beam. When the beam penetrates into the sample, its diameter is kept constant but its length is stretched along the propagation axis

due to refraction by a factor equal to the refractive index (small-angle approximation), resulting in a useful length for ablation inside the sample of $nz_B/2 \sim 15 \mu\text{m}$. The holes are processed sequentially one by one, each hole being ablated with a single laser pulse. We fabricated square arrays of 10×10 holes at the surface of fused silica, with a spatial period (pitch) of respectively $a = 5, 3,$ and $1.5 \mu\text{m}$. A large range of laser pulse energy is explored, in the sub-microjoule range. After fabrication, the surface of the sample is analyzed by SEM imaging after being coated with 5 nm of gold (Figures 2 and 3), enabling to measure the diameters of the holes. The side view is analyzed by optical microscopy (Figure 4), enabling to accurately measure their depth ($=$ length L).

3. Nanohole Arrays: Results and Discussion

3.1. Parametric Study {Energy, Pitch}

Figure 2 presents SEM pictures of the nanohole arrays written at the surface of the fused silica glass sample, for various pitches and laser pulse energy. The energy threshold for producing a hole, estimated by decreasing the pulse energy until no hole is realizable, is $E_{th} \sim 280 \text{ nJ}$ in our conditions. The measured beam intensity distribution (presented in Figure 1b) can be

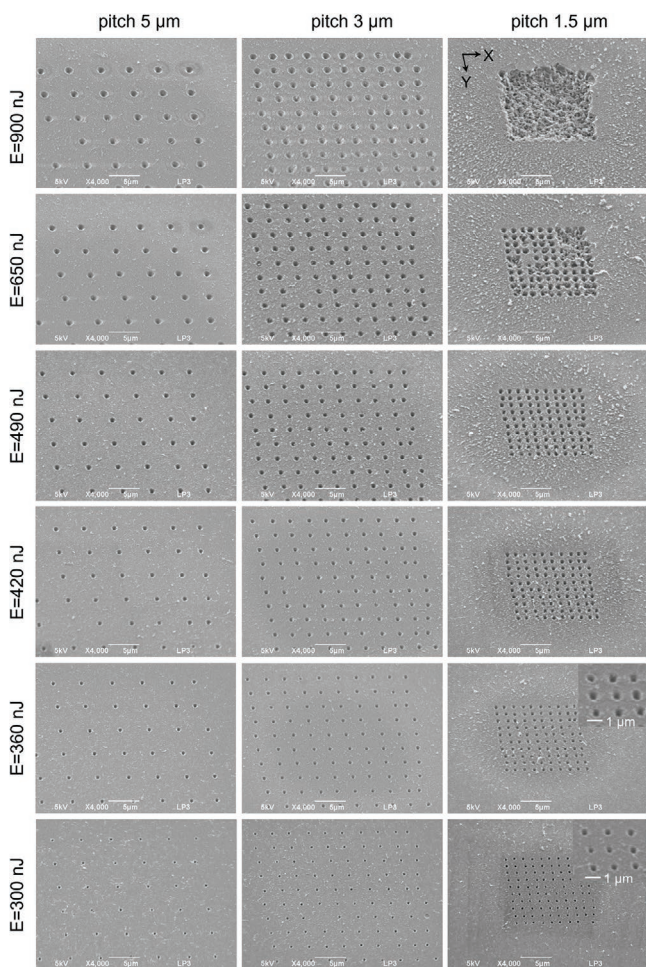


Figure 2. Arrays of 10×10 holes at the surface of fused silica (SEM images taken with a 40° tilt angle). The three columns correspond to arrays with decreasing spatial periodicity, with a pitch between holes of respectively $a = 5 \mu\text{m}$, $3 \mu\text{m}$, and $1.5 \mu\text{m}$. The laser pulse energy is indicated for each row. The scale bars ($5 \mu\text{m}$) are the same for all images, except for zoomed insets for energies of 360 nJ and 300 nJ .

translated into an absolute fluence distribution through a calibration procedure. As an example, for the measured threshold energy of $\approx 280 \text{ nJ}$, the peak fluence of the central core of the Bessel beam amounts $\approx 3.1 \text{ J cm}^{-2}$. This is comparable to values reported in the literature.^[39,40] However, one should keep in mind that this fluence value is the one that would be obtained if the beam were propagating in air (i.e., without any interaction with the material) and with no obstacles, which is obviously not the case here in ablation regimes. The most relevant parameter to the user is therefore the incident pulse energy.

Whatever the pitch, in a working energy range $E_{th} < E < 2E_{th}$, the entrance of each hole is free of any rims or molten matter. To highlight the capability of realization of such high-quality patterns by direct laser fabrication in air environment, we did not apply any post-treatment or even simple cleaning of the sample before or after laser ablation. This explains the scarce presence of surrounding ablation products and residual debris at the surface, mainly observed when the pitch is decreased. Overall, we observe a good reproducibility of the holes. For a

given energy, each hole of an array has the same diameter as a “single hole” (i.e., a hole drilled far away from any other ablated zone, not shown here) whatever the distance between adjacent holes. Within this energy range below twice the threshold, reducing the pitch to $3 \mu\text{m}$ and then down to $1.5 \mu\text{m}$ enables to obtain more densely-packed arrays of nanoholes, as desired. Note that the fluctuations of the distance between adjacent holes are attributed to accuracy limitations of the translation stages used to move the fused silica sample between irradiations.

Then, for the smallest pitch of $1.5 \mu\text{m}$ and if the energy is too high (see the case of energy $E = 900 \text{ nJ}$ for instance), the whole processed surface of the sample can be completely ablated with a very irregular morphology. This is obviously not desirable; however, by carefully adjusting the couple of parameters {energy, pitch}, small-size holes with various pitches are obtained for a large range of experimental conditions.

While Figure 2 shows SEM pictures recorded with a 40° tilt view angle, Figure 3a,b,c shows top-view images recorded at a 0° view angle. This enables to identify, for each hole, two distinct features: a dark round area in the very center, surrounded by a brighter circular zone. Considering the parallax effect due to the difference of view angles, the dimensions of the bright circular zone in Figure 3 perfectly match the diameters measured in Figure 2, that define the diameters of the entrance of the holes (D). The dark central zone, significantly smaller, is identified to be the diameter of the hole along its whole depth (d), in accordance with similar recent observations.^[39] Combining analyzes of tilted and nontilted images of Figures 2 and 3, we therefore obtain a strong indication that the entrances of the holes are funnel-shaped, as observed also by other authors in similar conditions.^[31,39–40] More details about this point are provided in Supporting Information Note 2.

3.2. Threshold-Based Analysis

The graph of Figure 3d shows how the hole diameter is controlled by the laser pulse energy. For the whole range of energies tested here, d and D are systematically measured for each of the 100 holes per case. The graph plots averaged values, with corresponding standard deviations (error bars). The evolution of d and D with the incident laser energy is quite different: the entrance diameter D rapidly decreases with a decrease of energy, while the hole diameter d shows less dependence (spanning in the range $190\text{--}330 \text{ nm}$). For a very low energy, these two values tend to merge, which would be the signature of a perfectly cylindrical hole without any funnel-shaped entrance.

Now, comparing beam dimensions to the hole diameter is instructive to interpret the results. Figure 3e presents the transverse profile (cross-section along X) of the experimental beam incident on the surface of the sample. Even if we severely truncated the beam after the axicon, the experimental beam profile remarkably well corresponds to a perfect non-truncated Bessel beam, as theoretically expected. The best numerical fit is obtained for an equivalent axicon angle of $\alpha' = 35.5^\circ$ (corresponding to a base angle of the axicon of $\alpha = 0.97^\circ$), very close to the expected value, and yielding a core diameter of $0.95 \mu\text{m}$ FWHM. The truncation also does not deteriorate the core-lobe

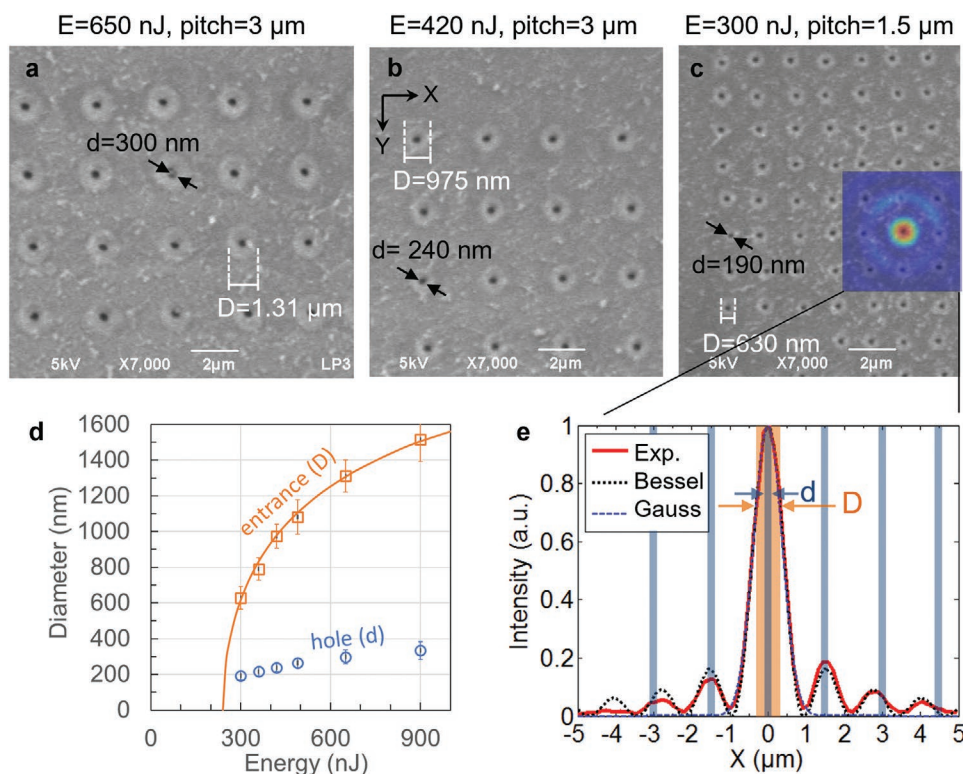


Figure 3. a,b,c) SEM images of the laser-processed holes with various combinations of energy and pitch. The hole diameter d (central dark area) and the entrance diameter D (surrounding white region) are indicated on the pictures. The experimental XY intensity of the tailored Bessel beam is also superimposed on image (c) in order to illustrate how the first lobe intercepts the neighboring hole when the pitch is reduced to $1.5 \mu\text{m}$. d) Evolution of measured diameters D and d with the incident laser energy. The values are averaged over the 100 holes per energy case and the error bars represent the standard deviation $\pm \sigma$ of our measurements (spanning in the ranges [63–121 nm] for D and [24–50 nm] for d). The solid line is a numerical fit (see text for details). (e) Transverse profile of the experimental beam (red), numerical fit of a non-truncated Bessel beam (black dotted), and numerical Gaussian fit of the central peak (blue dashed). The colored vertical regions represent the diameters D (in orange) and d (in blue) obtained for the case $E = 300 \text{ nJ}$. The blue region is reproduced every $1.5 \mu\text{m}$, in order to figure out the location of the neighboring holes.

intensity ratio compared to a regular Bessel beam (17% measured here).

It is now interesting to approximate the central peak to a Gaussian function. The numerical fit (in blue in Figure 3e) gives a beam waist of $w_0 = 0.74 \mu\text{m}$ (radius at $1/e^2$). This enables to use the Liu method^[41] to determine the surface ablation threshold: under the assumption that ablation is a strict threshold-based and deterministic mechanism,^[23,24] the diameter of the ablated crater should write: $w_0 \sqrt{2 \ln E/E_{th}}$. Using this expression to fit the experimental data of the entrance diameter D of the holes (solid line of Figure 3d) with w_0 and E_{th} as free parameters, we find an excellent agreement and we retrieve a surface ablation threshold of $E_{th} = 240 \text{ nJ}$, in reasonably good accordance with the experimental observation. Now regarding the hole diameter d , we observe a pronounced saturation when the pulse energy increases and, more importantly, a hole diameter that keeps always much smaller than the core of the Bessel beam. We attribute this effect to the impossibility for the ablated matter to be evacuated out of the hole in this regime of confined bulk ablation.^[42,43] Increasing the energy should yield a larger volume of ablated matter, but which is further redeposited on the walls of the hole, thus strongly limiting the increase of the obtained hole diameter. Therefore, we cannot expect a direct correspondence between the local

fluence profile and the hole diameter so that fitting the data for the hole diameter d with a threshold-based method would not be physically meaningful. The confinement of the interaction then offers, as a positive technological consequence, the ability to achieve sub-micrometer hole diameters without any specific effort of accurate energy adjustment. For illustration, the measured diameters d and D for the case $E = 300 \text{ nJ}$ and pitch $a = 1.5 \mu\text{m}$ (corresponding to Figure 3c) are reported on the beam profile displayed on Figure 3e. This highlights the suitability of Bessel beams for processing reliably holes whose diameters are far smaller than the laser writing wavelength.

We now discuss again the case when the combination {energy, pitch} is not optimized and can yield to uncontrolled ablation of the surface, as already observed in Figure 2. Due to the core-lobe intensity contrast, even if the energy largely overpasses the threshold for ablating the material surface with the central core of the beam (which is the case for energy $E = 900 \text{ nJ}$, corresponding to more than three times the threshold), the first lobe does not carry enough energy to induce ablation of a fresh surface. However, for series with the smallest pitch of $1.5 \mu\text{m}$, when the beam irradiates the next location during the point-by-point laser writing process, the surface is actually not fresh everywhere on surrounding regions, because previous holes preexist. Superposing the experimental

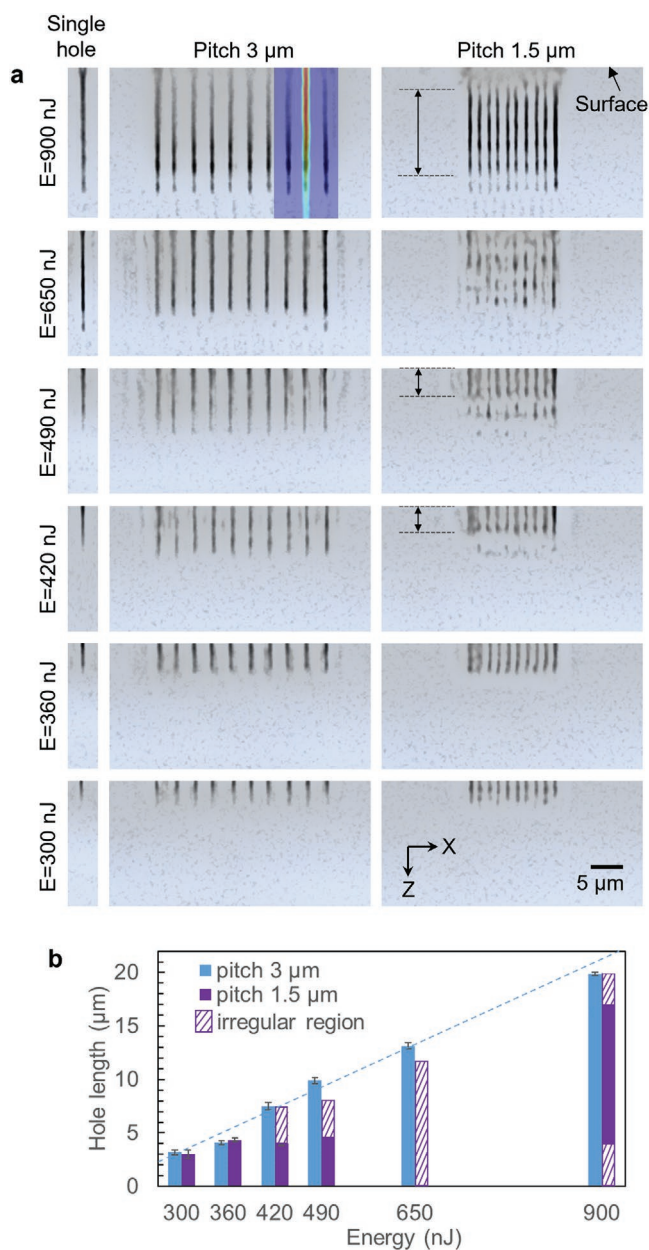


Figure 4. a) Side-views of the arrays of nanoholes (optical microscope images) for pitch 3 μm and 1.5 μm. For each energy, only 10 holes in the same Y plane are visible. A single hole is also shown on the left panel, for comparison. The scalebar of 5 μm holds for every image. The XZ intensity profile of the experimental beam is also superimposed on one hole on the first image, showing a good correspondence between the hole dimensions and the beam intensity distribution (beam coming from the top of the image). b) Evolution of the hole length with pulse energy for pitches of 3 μm and 1.5 μm. Each bar of the histogram represents the averaged value over the 10 holes measured for each case. The error bars stand for $\pm \sigma$ (standard deviation) of our measurements (spanning in the range [0.15–0.32 nm] for both pitches, except for the pitch 1.5 μm for $E \geq 420$ nJ). The appearance of detrimental crosstalk effects when the pitch decreases down to 1.5 μm (and for energy $E \geq 420$ nJ) yields to irregular morphologies along the holes depth, that are represented by hatched portions on the violet corresponding bars of the histogram.

beam intensity distribution to the SEM images (see Figure 3c) illustrates how the first lobe of the experimental beam overlaps neighboring holes, simply because the lobe radius (measured to be 1.52 μm) almost exactly corresponds to the pitch. Locally, the threshold (in other words, the minimum local energy density that triggers matter removal) is therefore significantly smaller than for a fresh surface (incubation effect) and lobe-induced ablation can occur. This effect reproduces for each shot of the array, yielding larger ablated volumes and matter removal over the whole area of the array. This is an inherent limitation to Bessel beams, that would require additional strategies to be overpassed. Nevertheless, this only appears for rather high energies, and leaves a reasonable processing range of energy $E_{th} < E < 2E_{th}$ for which the surface is free of such detrimental effect, even for the smallest pitch.

However, not only the surface ablation is disturbed by the neighbor holes. The closely-arranged preexisting holes actually can also affect the proper formation of the Bessel beam on its whole length beneath the sample surface, and therefore impact the proper engraving of the next hole. In this context, we name the “crosstalk effect” any perturbation of the propagation of the writing laser beam due to the presence of a collateral hole in close vicinity of the currently-processed one. This obviously includes the lobe-induced ablation described above, but also more delicate effects due to propagation distortions, that we examine in the next sections.

3.3. Controlling the Depth of Nanoholes

We now analyze the side views of the holes, presented in Figure 4a. These images are obtained by optical microscopy using a 100x, NA = 0.9 microscope objective, under white light transillumination through the lateral XZ face of the sample. Given the optical resolution which is typically $\lambda/2NA$, this obviously does not give access to the measurement of the hole diameters (nor at their entrance or along their depth), but it provides a convenient and accurate way to measure the depths of the holes.

Only the results of pitch 3 and 1.5 μm are presented for a conciseness purpose, since the results with pitch 5 μm are qualitatively similar to holes obtained with pitch 3 μm. The black tracks correspond to air holes, where matter has been ablated, as we have previously checked.^[33] Analyzing the 3 μm pitch series, deep holes with straight and reproducible profiles are obtained. Each hole of the array is the same as a single individual hole (displayed on the left) processed on a fresh material zone far away from any other hole. Importantly, no cracks or brittle fracture between holes is observed, whatever the energy in the range explored here, so that the holes are well defined and well separated. The use of Bessel beams proves here to be a direct convenient hole-writing solution, thanks to the good qualitative correspondence between the hole morphology (diameter, depth, cylindrical profile) and the intensity profile of the part of the experimental beam that enters inside the sample (also represented on the top line of the Figure). This is a major advantage, in particular over etching processes, for which maintaining a straight profile over depths of several micrometers can

be a technological challenge.^[9–12] The graph in Figure 4b shows how the hole lengths can be easily adjusted by tuning the laser pulse energy, with a roughly linear trend.

Decreasing the pitch to 1.5 μm and restricting the energy within a range $E_{th} < E < 1.5E_{th}$ simply yields more densely packed arrays of holes, as desired. No crosstalk effect is observed, and holes with straight and regular morphologies are obtained. As an example, using an energy of 360 nJ enables to produce holes of length $L = 4.1 \mu\text{m}$ and diameter $d = 215 \text{ nm}$ (aspect ratio = 19) for a pitch of 3 μm as well as 1.5 μm , with a good reproducibility (measured rms deviation of 4%). Further lowering the energy gives access to shorter holes, but the counterpart is a loss of reproducibility (see the error bars on the graph) because the energy used is very close to the ablation threshold, yielding higher sensitivity to pulse-to-pulse laser energy fluctuations. Note also here that using a truncated Bessel beam instead of a regular one enables us to benefit from a sharper falling edge of the tail of the beam (see Figure 1b) and thus to gain in the robustness of reproducibility regarding the hole length.

Still, for the 1.5 μm pitch series and now examining results for higher energies, the depth profile is affected, showing non-homogeneous and irregular hole morphologies. For moderate energies, the hole entrance is still of high quality (as already observed in Figures 2 and 3 for the energies of 420 nJ and 490 nJ) but the end of the holes is affected. The corresponding regions are represented by hatched portions on the violet corresponding bars of the histogram of Figure 4b. For the highest energy of 900 nJ for which the surface is totally ablated, the remaining length of the holes is surprisingly unaffected (except on the last micrometers). This feature, a priori unexpected, illustrates here a crucial advantage of Bessel beams over Gaussian beams for robust processing capability of nano-hole arrays: since the laser energy is delivered “from the side” (with the angle θ) all along the hole depth with the lobe rings acting as the energy reservoir, the machining of holes below the surface is still efficient (when using high energies) even if the surface is destroyed. Besides, postpolishing of the sample surface to remove the first micrometers of matter should enable to access the holes and thus reveal them at the surface. For holes produced with a lower energy, such an approach could also constitute a convenient way to remove the funnel-shaped entrance, as well as bring additional freedom to the final holes lengths by removing calibrated material thicknesses.

3.4. Crosstalk Effect: Numerical Investigation

In this section, we investigate in more details the crosstalk effect, responsible of a current limitation on the achievable density of the produced close-packed arrays of holes. For energetic conditions that are too low to sustain the side-lobe ablation effect already discussed, at least two other reasons could be invoked. The first one is optical: despite the robustness of propagation of Bessel beams against obstacles, also known as “self-healing” capabilities,^[44] the presence of the previous holes can still perturb the wavefront propagation. This may cause that the micro-Bessel beam does not form properly anymore, thereby affecting the processing of the next hole. Since hole diameter

and depth depend on energy, as characterized previously, obstacles of growing dimensions affect the beam propagation upon increase of laser pulse energy. The second reason, more minor, is the possible modification of the material properties between the holes (e.g., densification, index change, structural reorganization, shear stress, etc.). This may also induce uncontrolled material fracture, thus preventing the processing of straight and regular holes at high energy. Such modifications would not be easily detectable by optical microscopy, but they could be evidenced by more advanced material analysis tools, which is out of the scope of the present paper. Here, we propose a numerical study of optical propagation to investigate the first reason. We simulate the behavior of the truncated micro-Bessel beam when its propagation is perturbed by the presence of a regular arrangement of pre-existing holes.

The 2D spatial distribution of holes at the surface of the sample, therefore, requires 3D description and computing. In the framework of Fresnel propagation model, the optical field at a position z is depicted by a 2D complex amplitude $A(x, y, z)$ and can be decomposed in the Fourier space as a sum of plane waves (the “angular spectrum”), each plane wave being defined by a wavevector $\vec{k} = (k_x, k_y, k_z)$. If the optical field encounters obstacles, then $A(x, y, z)$ is multiplied by the corresponding complex transmittance function $T(x, y)$. This enables us to depict within the same formalism pure phase elements (the axicon, the air/glass interface) as well as obstacles that affect the amplitude (annular aperture, pre-existing nano-holes) placed in any plane z along propagation. In the Fourier space, propagation along a distance dz is calculated by multiplying the angular spectrum by the Fourier Kernel propagator $P(x, y, dz) = e^{ik_z dz} = \exp[i dz \sqrt{k^2 - k_x^2 - k_y^2}]$. Note that this Fresnel propagator of plane waves is valid even if paraxial conditions are not fulfilled. Note also that we neglect here the effects of the spectral bandwidth of our laser pulse. The optical field after propagation then writes $A(x, y, z + dz) = \mathcal{F}^{-1} \{ P(x, y, dz) \cdot \mathcal{F} \{ A(x, y, z) \cdot T(x, y) \} \}$, where \mathcal{F} denotes the Fourier transform. The 3D complex amplitude along propagation is obtained by applying this algorithm step by step along z , and the intensity is finally obtained by $I(x, y, z) = |A(x, y, z)|^2$.

Results are presented in Figure 5. Case (a) represents the truncated micro-Bessel beam that propagates at the air/glass interface without introduction of any obstacle, as a reference. Cases (b), (c), and (d) simulate the propagation of the beam that will process the next hole, when approximately the first half of the 10×10 array of holes is already fabricated. Simulations are run for the case of energy $E = 490 \text{ nJ}$, taking the experimentally measured values for hole diameter ($d = 265 \text{ nm}$) and hole length ($L = 10.0 \mu\text{m}$). Considering that a lateral hole is mainly a source of energy loss, we depict numerically one hole by a cylindrical pattern whose transmission is zero (white disks and tracks on the Figure) as in Ref. [45]. Also, for simplicity, no funnel-shaped entrance is considered here. Since 2D calculations with high numerical sampling require large computation time resources, the simulation includes a transformation optics approach with corresponding virtual obstacles affecting the Bessel beam before demagnification. Then, we do not expect that the detailed features of near-field diffraction effects are accurately depicted by the simulation. However, as we will show, the way the lateral masking effects can affect the

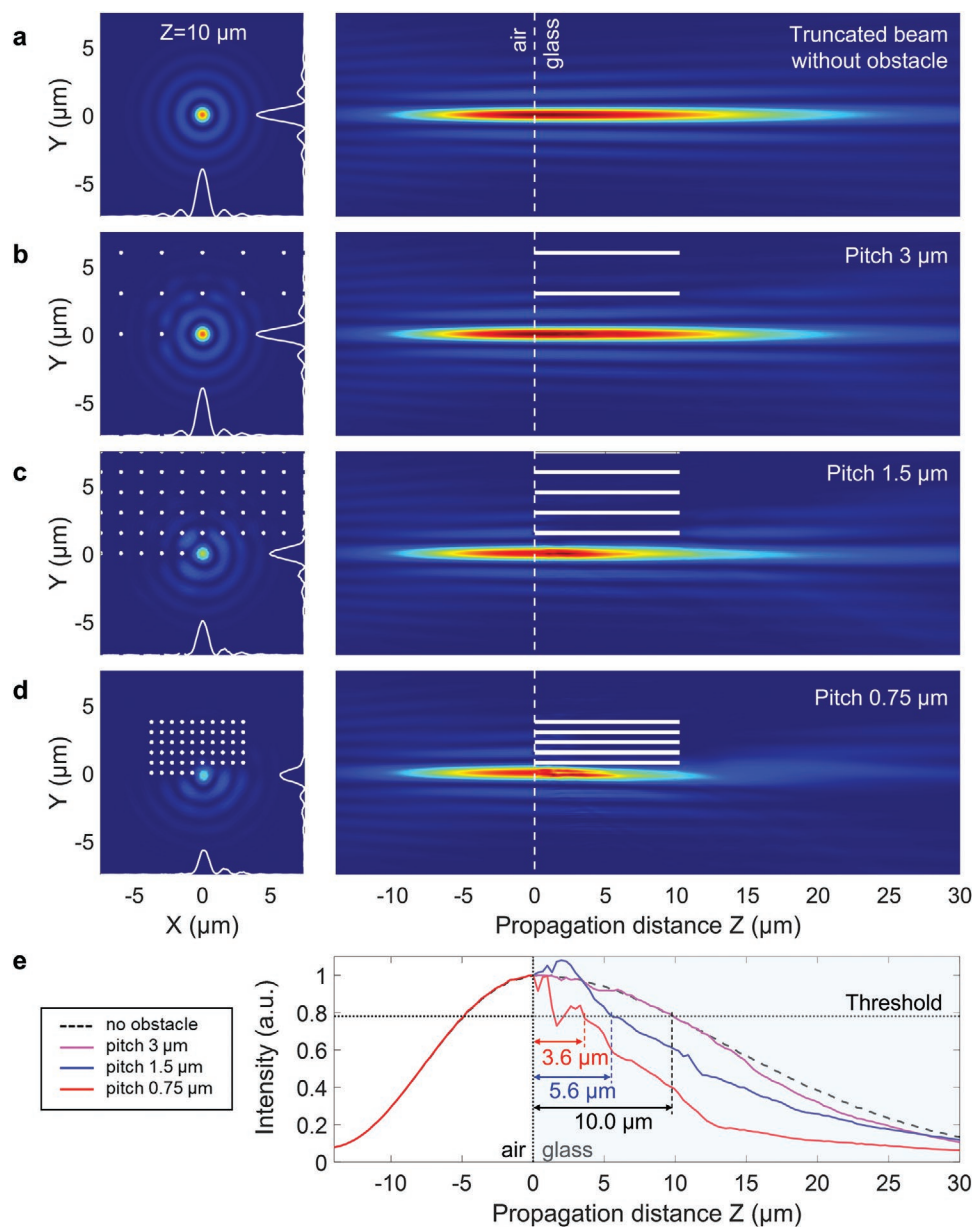


Figure 5. Numerical study of crosstalk: simulations of beam propagation and distortions in presence of preexisting holes at the surface of the sample, for decreasing pitches. a) no obstacle, b) pitch $a = 3 \mu\text{m}$, c) pitch $a = 1.5 \mu\text{m}$, d) pitch $a = 0.75 \mu\text{m}$. The coordinate $Z = 0$ is the surface of the fused silica glass sample, placed at the maximum intensity of the incoming beam. All images are normalized to this value and they are therefore directly comparable. The XY beam intensities (left panel) are taken at $Z = 10 \mu\text{m}$; this enables to compare the beam distortions and drop of intensity at the end of the hole for each case studied. The YZ intensity distributions (right panel) display the beam propagation. The white disks and the white tracks represent the preexisting holes. The intensity profiles along Z are plotted on the graph e) for all cases. By direct comparison with experiments, the ablation threshold is obtained for a normalized intensity of 78%.

general delivery and dimensions of the intense elongated beam remains accessible with these simplifications.

Without obstacle, and by comparison to the measured hole depth, the local intensity at $Z = 10 \mu\text{m}$ defines the threshold for ablation (see profiles in Figure 5e). For a pitch of $3 \mu\text{m}$ (case b), the beam is very little perturbed. The expected hole length is unchanged, perfectly matching with the experimental measurements reported in Figure 4. Decreasing the pitch to $1.5 \mu\text{m}$ and then further to $0.75 \mu\text{m}$ for better illustration yields several

beam distortions, amongst which: intensity modulations and local over-intensities, increased beam divergence associated with a loss of the axial symmetry of the intensity distribution, but also, and more importantly, shortening of the useful length of the Bessel beam for ablation. Indeed, since the energy that forms the tail of the Bessel beam is mainly contained in the outer lobe rings at shorter Z distances, their perturbation by the previous lateral holes (even at a radial distance larger than the pitch) induces spatial reorganization of energy that prevents to

form properly an intense central core at the tail of the beam. For the 1.5 μm pitch (case c), a premature drop in the intensity of the Z-profile is observed, that yields an expected shorter hole depth, with only the first 5.6 μm overpassing the threshold. This numerical result is in good agreement with the observation of Figure 4a for the case 490 nJ, where only the first $\approx 5 \mu\text{m}$ of the holes are straight and reproducible (see also the height of the nonhatched portion of the histogram bar in Figure 4b). The same kind of effect is observed for the 420 nJ energy case. Now, further lowering the energy yields a decrease in the hole diameter and length, thereby diminishing perturbations of the beam, so that the length of the hole is maintained, even for small pitches (simulations not shown here). Such evolution is fully in line with experimental observations and measurements. Remembering that we explore here the condition of front-side ablation, which is often less favorable than bulk or rear-side processing^[45] but offers larger versatility, these results illustrate the key benefit of Bessel beams in their stability range for robust processing of nanohole arrays.

Having identified the existence of crosstalk effects defining limit in the process, beam shaping solutions for future developments can be proposed, like apodization of the side lobes,^[46,47] replacement of Bessel beams by droplets beams^[48] or needle beams.^[49] More generally, any solution of beam engineering to work with asymmetric condition and, thus, provide the possibility to restrict the beam propagation to regions free of previous features would be of high interest. This would also bring the possibility to further reduce the pitch to fractions of visible wavelengths, in view of further design and fabrication of nanocomponents for visible light.

4. Conclusion

In summary, we fabricated and characterized square arrays of deep holes by ultrashort pulse ablation of the surface of fused silica under ambient air. We demonstrated that length-tailored Bessel beam ablation is a relevant approach for processing closely-spaced nanohole arrays with large and controllable depths and straight profiles. A complete analysis of holes (diameter, depth, entrance, regularity) was carried and interpreted with respect to the ablation threshold and laser beam intensity distribution. Hole diameters less than 250 nm (which is roughly one-third of the writing laser wavelength) over a depth of several micrometers are obtained, arranged in two-dimensional arrays with a pitch down to 1.5 μm . The influence of the spatial periodicity of the arrays on the stability of the propagation of the customized Bessel beam inside the material depth was investigated, both experimentally and numerically. Upon the careful adjustment of a couple of parameters {energy, pitch}, reproducible arrays of nanoholes with aspect ratio in the range 5–30 are accessible. The dimensions and pitch attained here thus already open the possibility to design and write components for the mid-infrared spectral range. Further downscaling of the patterns and specifically further densification of the arrays of holes should be accessible either by changing the writing wavelength to enhance the optical resolution and/or implement complementary beam-shaping solutions.

This technological demonstration is a critical step towards agile laser-fabrication of advanced devices for a range of applications in integrated photonics. Indeed, since the point-by-point laser writing tool offers intrinsically the ability to deliver energy over flexible geometries, it constitutes a unique route for rapid prototyping of patterns of higher complexity level, for instance, intricate structures with varying hole diameters, lengths, and density across the same substrate, produced on a single laser process. Moreover, while the results demonstrated here concentrate on fused silica as a model glass substrate, the universality of the ultrashort laser ablation response of bandgap solids enable us to envision an approach applicable to a broad range of target materials. An important interest of arrays of deep and cylindrical “air holes” is for light-confining structures (Bragg mirrors, photonic crystals) at the surface of photonic integrated circuits, for example on lithium niobate chips,^[50] adapted from the concept of laser-writing inside optical fiber core.^[51] Moreover, semiconductors are accessible upon adjustment of the laser wavelength to match their transparency spectral region.^[52] This could open new opportunities to fabricate silicon photonic integrated devices by index engineering based on nanohole assembly laser writing.^[53,54]

Aside the spatial resolution, process throughput is an important aspect in comparison with more traditional nanofabrication tools. While the demonstration of our flexible laser-ablation-based technique in atmospheric conditions may appear limited in comparison to lithography-based production methods, the current advent of kilowatt ultrashort laser sources must allow to rapidly envision massive parallelization of the writing process^[55] leading to the vision of an attractive novel modality for fast, versatile, low-environmental-impact and cost-effective nanoprocessing of optical materials.

Acknowledgements

The authors thank E. André for fabricating the annular apertures. This project has received financial support from CNRS through the MITI interdisciplinary programs. French Ministry of Research and High Education, Region Provence-Alpes-Côte d'Azur, Department of Bouches-du-Rhône, City of Marseille, CNRS, and Aix-Marseille University were gratefully acknowledged for funding the ASUR platform.

Conflict of Interest

The authors declare no conflict of interest.

Data Availability Statement

The data that support the findings of this study are available from the corresponding author upon reasonable request.

Keywords

Bessel beams, fused silica, laser processing, nanohole arrays

Received: October 5, 2022
Revised: December 14, 2022
Published online:

- [1] C. Genet, T. W. Ebbesen, *Nature* **2007**, *445*, 39.
- [2] J. W. Menezes, J. Ferreira, M. J. L. Santos, L. Cescato, A. G. Brolo, *Adv. Funct. Mater.* **2010**, *20*, 3918.
- [3] Y. Xu, P. Bai, X. Zhou, Y. Akimov, C. E. Png, L.-K. Ang, W. Knoll, L. Wu, *Adv. Opt. Mater.* **2019**, *7*, 1801433.
- [4] P. Cheben, R. Halir, J. H. Schmid, H. A. Atwater, D. R. Smith, *Nature* **2018**, *560*, 565.
- [5] K. Bi, Q. Wang, J. Xu, L. Chen, C. Lan, M. Lei, *Adv. Opt. Mater.* **2021**, *9*, 2001474.
- [6] S. Walia, C. M. Shah, P. Gutruf, H. Nili, D. H. Chowdhury, W. Withayachumnankul, S. Sriram, *Appl. Phys. Rev.* **2015**, *2*, 011303.
- [7] C. Soukoulis, M. Wegener, *Nat. Photonics* **2011**, *5*, 523.
- [8] A. Degiron, H. J. Lezec, W. L. Barnes, T. W. Ebbesen, *Appl. Phys. Lett.* **2002**, *81*, 4327.
- [9] S. Ni, E. J. W. Berenschot, P. J. Westerik, M. J. de Boer, R. Wolf, H. Le-The, H. Gardeniers, N. R. Tas, *Microsyst. Nanoeng.* **2020**, *6*, 25.
- [10] E. D. Le Boulbar, C. J. Lewins, D. W. E. Allsopp, C. R. Bowen, P. A. Shields, in *Microelectronic Engineering*, Elsevier Science Pub. Co., Amsterdam **2016**, Vol. 153, pp. 132-136.
- [11] O. Yavuzcetin, B. Ozturk, D. Xiao, S. Sridhar, *Opt. Mater. Express.* **2011**, *1*, 1262.
- [12] G. W. Burr, S. Diziaini, M. P. Bernal, *Opt. Express* **2008**, *16*, 6302.
- [13] A. Ródenas, M. Gu, G. Corrielli, P. Paiè, S. John, A. K. Kar, R. Osellame, *Nat. Photonics* **2019**, *13*, 105.
- [14] Y. Li, K. Itoh, W. Watanabe, K. Yamada, D. Kuroda, J. Nishii, Y. Jiang, *Opt. Lett.* **2001**, *26*, 1912.
- [15] A. She, S. Zhang, S. Shian, D. R. Clarke, F. Capasso, *Opt. Express* **2018**, *26*, 1573.
- [16] J. Bonse, S. V. Kirner, J. Krüger, Laser-Induced Periodic Surface Structures (LIPSS) in *Handbook of Laser Micro- and Nano-Engineering* (Ed. K. Sugioka,) Springer, Cham **2021**, Vol. 2, pp. 879–936.
- [17] R. Rudenko, J. P. Colombier, T. E. Itina, R. Stoian, *Adv. Opt. Mater.* **2021**, *9*, 2100973.
- [18] G. D. Tsibidis, C. Fotakis, E. Stratakis, *Phys. Rev. B.* **2015**, *92*, 041405(R).
- [19] E. Mcleod, C. Arnold, *Nat. Nanotechnol.* **2008**, *3*, 413.
- [20] D. Grojo, L. Boarino, N. De Leo, R. Rocci, G. Panzarasa, P. Delaporte, M. Laus, K. Sparnacci, *Nanotechnology* **2012**, *23*, 485305.
- [21] Z. Z. Li, L. Wang, H. Fan, Y. H. Yu, Q. D. Chen, S. Juodkazis, H. B. Sun, *Light Sci Appl* **2020**, *9*, 41.
- [22] A. P. Joglekar, H. Liu, G. J. Spooner, E. Meyhöfer, G. Mourou, A. J. Hunt, *Appl. Phys. B.* **2003**, *77*, 25.
- [23] N. Sanner, O. Utéza, B. Chimier, M. Sentis, P. Lassonde, F. Légaré, J. C. Kieffer, *Appl. Phys. Lett.* **2010**, *96*, 071111.
- [24] M. Garcia-Lechuga, O. Utéza, N. Sanner, D. Grojo, *Opt. Lett.* **2020**, *45*, 952.
- [25] P. Balling, J. Schou, *Rep. Prog. Phys.* **2013**, *76*, 036502.
- [26] M. Lebugle, N. Sanner, N. Varkentina, M. Sentis, O. Utéza, *J. Appl. Phys.* **2014**, *116*, 063105.
- [27] M. Lebugle, N. Sanner, O. Utéza, M. Sentis, *Appl. Phys. A.* **2014**, *114*, 129.
- [28] J. Hernandez-Rueda, N. Götte, J. Siegel, M. Soccio, B. Zielinski, C. Sarpe, M. Wollenhaupt, T. A. Ezquerro, T. Baumert, J. Solis, *ACS Appl. Mater. Interfaces* **2015**, *7*, 6613.
- [29] N. Götte, T. Winkler, T. Meinl, T. Kusserow, B. Zielinski, C. Sarpe, A. Senftleben, H. Hillmer, T. Baumert, *Optica* **2016**, *3*, 389.
- [30] J. F. Herbstman, A. J. Hunt, *Opt. Express.* **2010**, *18*, 16840.
- [31] M. K. Bhuyan, F. Courvoisier, P. A. Lacourt, M. Jacquot, R. Salut, L. Furfaro, J. M. Dudley, *Appl. Phys. Lett.* **2010**, *97*, 081102.
- [32] R. Stoian, J. P. Colombier, *Nanophotonics* **2020**, *9*, 4665.
- [33] X. Liu, N. Sanner, M. Sentis, R. Stoian, W. Zhao, G. Cheng, O. Utéza, *Appl. Phys. A* **2018**, *124*, 206.
- [34] J. H. McLeod, *J. Opt. Soc. Am.* **1954**, *44*, 592.
- [35] R. M. Herman, T. A. Wiggins, *J. Opt. Soc. Am. A* **1991**, 932.
- [36] A. Müller, M. C. Wapler, U. Wallrabe, *Opt. Express* **2017**, *25*, 22640.
- [37] O. Brzobohaty, T. Cizmar, P. Zemanek, *Opt. Express* **2008**, *16*, 12688.
- [38] X. Liu, Q. Li, A. Sikora, M. Sentis, O. Utéza, R. Stoian, W. Zhao, G. Cheng, N. Sanner, *Opt. Express.* **2019**, *27*, 6996.
- [39] T. Chen, G. Zhang, Y. Wang, X. Li, R. Stoian, G. Cheng, *Micromachines* **2020**, *11*, 671.
- [40] S. Lavin-Varela, S. Madden, K. Yan, M. Ploschner, A. V. Rode, L. Rapp, *Opt. Express.* **2022**, *30*, 6016.
- [41] J. M. Liu, *Opt. Lett.* **1982**, *7*, 196.
- [42] S. Juodkazis, K. Nishimura, S. Tanaka, H. Misawa, E. G. Gamaly, B. Luther-Davies, L. Hallo, P. Nicolai, V. T. Tikhonchuk, *Phys. Rev. Lett.* **2006**, *96*, 166101.
- [43] J. Del Hoyo, R. Meyer, L. Furfari, F. Courvoisier, *Nanophotonics* **2021**, *10*, 1089.
- [44] M. McLaren, T. Mhlanga, M. J. Padgett, F. S. Roux, A. Forbes, *Nat. Commun.* **2014**, *5*, 3248.
- [45] F. Courvoisier, J. Zhang, M. K. Bhuyan, M. Jacquot, J. M. Dudley, *Appl. Phys. A.* **2013**, *112*, 29.
- [46] F. He, J. Yu, Y. Tan, W. Chu, C. Zhou, Y. Cheng, K. Sugioka, *Sci. Rep.* **2017**, *7*, 40785.
- [47] G. Di Domenico, G. Ruocco, C. Colosi, E. DelRe, G. Antonacci, *Sci. Rep.* **2018**, *8*, 17178.
- [48] J. Tang, J. Ren, K. Y. Han, *Nanophotonics* **2019**, *8*, 2111.
- [49] R. Grunwald, M. Bock, *Adv. Phys.* **2020**, *5*, 1736950.
- [50] M. Li, J. Ling, Y. He, U. A. Javid, S. Xue, Q. Lin, *Nat. Commun.* **2020**, *11*, 4123.
- [51] K. Mahmoud Aghdami, A. Rahnama, E. Ertorer, P. R. Herman, *Nat. Commun.* **2021**, *12*, 6344.
- [52] M. Chambonneau, D. Grojo, O. Tokel, F. Ö. Ilday, S. Tzortzakos, S. Nolte, *Laser Photonics Rev.* **2021**, *15*, 2170059.
- [53] K. Q. Peng, X. Wang, L. Li, X. L. Wu, S. T. Lee, *J. Am. Chem. Soc.* **2010**, *132*, 6872.
- [54] I. E. Khodasevych, L. Wang, A. Mitchell, G. Rosengarten, *Adv. Opt. Mater.* **2015**, *3*, 852.
- [55] R. Bowman, N. Muller, X. Zambrana-Puyalto, O. Jedrkiewicz, P. Di Trapani, M. J. Padgett, *Eur. Phys. J.: Spec. Top.* **2011**, *199*, 159.